Nanoscale Advances

ROYAL SOCIETY OF CHEMISTRY

PAPER

View Article Online
View Journal | View Issue

Cite this: *Nanoscale Adv.*, 2025, **7**, 7015

First-principles investigation of the electronic, piezoelectric and transport properties of InSeX (X = Cl, Br, I) monolayers

D. Vo Dat, [ab] Tuan V. Vu, [ab] A. I. Kartamyshev, [ab] Thi H. Ho, [ab] Hoang-Thinh Do,[c] Vu Khac Hoang Bui,[d] Phan T. H. Linh[e] and Nguyen D. Hien *[fg]

First-principles calculation was performed to study InSeX (X = Cl, Br, and I) monolayers, which are formed by the breaking of In–In bonds in InSe monolayers through full halogenation. The isolated InSeX monolayers have Se–In–X stacking configuration with a buckled honeycomb structure maintained by newly formed Se-sp^3 hybrid orbitals. InSeX (X = Cl, Br, and I) monolayers have good mechanical properties with Young's modulus in the range of 28.69–33.44 N m^{-1} and a Poisson's ratio of nearly 0.30. Their in-plane structures are expected to be highly isotropic due to the independence of elastic parameters on the angle of applied strains. A high carrier concentration (10^{20} cm^{-3}) and scattering mechanisms greatly reduce the mobility of these monolayers, especially at high temperature. However, the InSeI monolayer appears to be a promising material because its electron mobility is rather high, 10.82–217.33 cm^2 V^{-1} s^{-1}, at a temperature of 50–400 K. InSeX (X = Cl, Br, and I) monolayers are also promising piezoelectric materials with high in-plane piezoelectric coefficients e_{11} in the range of 3.34–5.60 × 10^{-10} C m^{-1} and d_{11} of 14.90–33.50 pm V^{-1}. The current study provides the mechanism of how isolated InSeX (X = Cl, Br, and I) monolayers are formed and stabilized, which is useful to expand the new subclass of 2D materials by applying the same procedure for group XIII monochalcogenides (MX, where M = B, Al, Ga, In, Tl and X = S, Se, Te). InSeX (X = Cl, Br, and I) monolayers are also promising for a wide range of applications because of the broad tunability of the bandgap (1.36–2.94 eV), band edge positions, and work function (4.80–7.80 eV).

Received 10th June 2025
Accepted 1st September 2025

DOI: 10.1039/d5na00567a

rsc.li/nanoscale-advances

1 Introduction

Indium selenide (InSe) monolayers have become one of the most promising two-dimensional (2D) materials, attracting growing interest in recent research. A theoretical study in 2015 highlighted their potential by predicting a high electron mobility of approximately 10^3 cm^2 V^{-1} s^{-1}, indicating suitability for field-effect transistor (FET) applications.[1] Since then, steady progress has been made particularly from 2018 onward in synthesizing uniform, phase-pure InSe monolayers with controlled thickness and large lateral dimensions.[2–5]

InSe monolayers are promising due to their high intrinsic carrier mobility and moderate bandgap (1.26 eV), making them suitable for a variety of electronic and optoelectronic applications.[2,6,7] Previous studies have demonstrated their potential in field-effect transistors (FETs).[8,9] For instance, Sucharitakul *et al.* reported that multilayer InSe FETs exhibit ultrahigh room-temperature field-effect mobility exceeding 10^3 cm^2 V^{-1} s^{-1}.[1] Theoretically, monolayer InSe transistors have been shown to benefit from strain-induced enhancements in photoresponse (0.18 A W^{-1}) and external quantum efficiency (62.5%).[10] Additionally, Tamalampudi *et al.* demonstrated that few-layer InSe-based photodetectors exhibit broadband photoresponse and high responsivity, reaching 12.3 A W^{-1} at 450 nm.[11] Beyond optoelectronics, InSe monolayers also hold promise in gas sensing applications due to their large surface-to-volume ratio and tunable electronic structure.[12] First-principles studies indicate strong interaction between InSe and polar gases (*e.g.*, NO_2, NH_3, H_2S, and CO), owing to the Se-dominated valence band located near the Fermi level.[13] Experimental study showed that UV-activated InSe-based chemiresistors have achieved

[a]*Laboratory for Computational Physics, Institute for Computational Science and Artificial Intelligence, Van Lang University, Ho Chi Minh City, Vietnam. E-mail: dat.vd@vlu.edu.vn*

[b]*Faculty of Mechanical, Electrical, and Computer Engineering, Van Lang School of Technology, Van Lang University, Ho Chi Minh City, Vietnam*

[c]*Laboratory for HI-TECH Applications, Institute for Computational Science and Artificial Intelligence, Van Lang University, Ho Chi Minh City, Vietnam*

[d]*Laboratory for Advanced Nanomaterials and Sustainable Energy Technologies, Institute for Computational Science and Artificial Intelligence, Van Lang University, Ho Chi Minh City, Vietnam*

[e]*Nha Trang Central Ethnic Minority Pre-university, Nha Trang City, Khanh Hoa Province, Vietnam*

[f]*Institute of Research and Development, Duy Tan University, Da Nang 550000, Vietnam. E-mail: nguyendinhhien2@duytan.edu.vn*

[g]*School of Engineering & Technology, Duy Tan University, Da Nang 550000, Vietnam*

remarkable sensitivity and selectivity.[14] For example, few-layer InSe sensors demonstrated reversible NO_2 detection with a detection limit of 0.98 ppb and a rapid response time of about 41 s for 50 ppm NO_2 at room temperature.[14] For solar energy applications, the narrow bandgap of InSe monolayers enables strong absorption of visible light.[15] The pristine monolayer InSe is predicted to achieve solar-to-hydrogen (STH) efficiencies of 1–6% for photocatalytic water splitting.[16] Notably, the InSe/graphene photoanode was determined to have a high photocurrent density exceeding 10 mA cm^{-2} at 1.23 V *vs.* RHE under illumination,[17] suggesting effective hydrogen evolution. In photovoltaic applications, InSe can work effectively as either an absorber or a window layer in type-II van der Waals heterostructures. For instance, simulations of an InSe/tellurene bilayer predict a power conversion efficiency of approximately 13%, highlighting its promise in next-generation solar cells.[18]

To further enhance the performance of InSe-based devices, various material engineering strategies have been proposed. Doping, both substitutional and adsorptive, can significantly tune the electronic structure. For example, first-principles studies show that group-IV dopants (*e.g.*, Si and Ge) make InSe metallic, while group-V dopants (*e.g.*, P and As) reduce the bandgap and can even introduce magnetism.[19] Similar effects have also been found when AlN, AsP and GaN monolayers are substitutionally doped or hydrogenated.[20,21] Moreover, substitution of group IVA and *VIA* atoms, including Br, causes modification of the bandgap and electronic structure of the β-GeSe monolayer.[22,23] Strain engineering is another effective method, capable of inducing an indirect-to-direct bandgap transition and narrowing the bandgap under tensile strain – thereby tuning optical and electronic properties.[24] Heterostructure formation with other 2D materials also offers performance gains. For example, van der Waals InSe/In_2SSe structures have demonstrated enhanced on-state currents and faster switching speeds in sub-5 nm transistors compared to pristine InSe.[25] Surface functionalization and charge-transfer doping have similarly shown strong potential. Notably, anchoring Lewis-acidic species like Ti^{4+} onto InSe forms planar p-type complexes,[13] and coating InSe with a thin indium overlayer has experimentally led to a 59-fold increase in electron mobility and a 3-fold enhancement in photodetector responsivity due to improved charge transfer.[26]

To broaden the scope of InSe-based applications, Yagmurcukardes *et al.* attempted full fluorination of InSe monolayers, resulting in a Se–In–F stacking structure rather than the typical Se–In–In–Se configuration.[27] However, this fully fluorinated InSeF monolayer was found to be structurally unstable, undergoing phase transformations under further modifications to achieve a stable structure. A more successful approach was demonstrated by Rui Guo *et al.* (2023), who showed that GaSe monolayers could be converted into stable GaSeX (X = Cl, Br, and I) monolayers *via* halogenation.[28]

Inspired by these results, the current study investigates fully halogenated InSeX (X = Cl, Br, I) monolayers using first-principles calculations. The structural stability of these systems is confirmed through binding energy analysis and phonon dispersion calculations. Electronic structure and orbital-resolved (fat band) analyses reveal how halogenation disrupts the In–In bonds in pristine InSe, stabilizing Se–In–X monolayers in a buckled honeycomb configuration. Due to the non-centrosymmetry of these configurations, their piezoelectric coefficients were calculated. Additionally, the transport properties were examined across varying carrier concentrations and temperatures. This study provides valuable insights into the tunability of the bandgap, band edge positions, and work function and establishes clear relationships between carrier mobility, temperature, carrier density, and dominant scattering mechanisms.

2 Computational details

First-principles calculations were performed using the Vienna *ab initio* simulation package (VASP).[29,30] The interactions between electrons and ions were described using the projector augmented-wave (PAW) method,[31,32] and the exchange–correlation energy was treated within the framework of the generalized gradient approximation (GGA) using the Perdew–Burke–Ernzerhof (PBE) functional.[33] Based on the buckled honeycomb structure of the pristine InSe monolayer,[34] the atomic models of InSeX (X = Cl, Br, I) monolayers were constructed and fully relaxed at the PBE level. A vacuum spacing of 25 Å was introduced along the out-of-plane direction to eliminate interactions between neighboring images.[35] Due to the presence of rather heavy atoms (In and I) and associated relativistic effects, spin–orbit coupling (SOC) was included in separate calculations (denoted PBE + SOC) to assess its impact on bandgap values. To account for dispersion interactions inherent in buckled structures, the Grimme DFT-D3 van der Waals correction[36] was applied throughout the structural optimization and energy calculations. It has been proven that the PBE bond length is very close to the results from hybrid functional or experiments.[37–42] Meanwhile, structural optimization using the HSE06 functional requires expensive computational cost. Therefore, the structural optimization in this study was performed using the PBE method together with the vdW correction. For improved accuracy in the electronic properties, the screened hybrid Heyd–Scuseria–Ernzerhof (HSE06) functional,[43] incorporating 25% Hartree–Fock exchange, was used to calculate electronic band structures and bandgaps for the optimized geometries. All calculations employed a plane-wave energy cutoff of 500 eV. The Brillouin zone was sampled using a $15 \times 15 \times 1$ Monkhorst–Pack[44] $k-$ point mesh for the primitive unit cell. The electronic self-consistency loop was converged to an energy threshold of 10^{-6} eV, while structural relaxation was performed until the residual Hellmann–Feynman forces on all atoms were below 10^{-4} eV AA^{-1}, with the total stress minimized accordingly.

Phonon dispersion calculations were performed to verify the dynamic stability of the InSeX (X = Cl, Br, I) monolayers. The second-order interatomic force constants were computed using the finite-displacement method as implemented using the PHONOPY package.[45] A $6 \times 6 \times 1$ supercell was used to calculate the force constants and derive phonon spectra. Charge carrier mobilities were estimated by solving the Boltzmann transport equation under the relaxation time approximation

(RTA), incorporating four dominant scattering mechanisms: acoustic deformation potential (ADP) scattering, polar optical phonon (POP) scattering, ionized impurity (IMP) scattering, and piezoelectric (PIE) scattering. The relevant physical parameters – including elastic coefficient tensor C_{ij} and piezoelectric strain coefficient e_{ij} were extracted from both DFT (GGA-PBE) and density functional perturbation theory (DFPT) calculations.[46] Scattering rates for each mechanism were computed by interpolating the DFT band structure and evaluating the corresponding coupling matrix elements using the AMSET code.[47] Matthiessen's rule[48] was applied to combine the contributions from individual scattering channels and obtain the total carrier mobility.

3 Results and discussion

3.1 Geometry and structural stability of InSeX (X = Cl, Br, and I) monolayers

It is well-known that the pristine InSe monolayer belongs to the D_{3h} space group,[49] where covalent bonding holds four sublayers of In and Se atoms in the order of Se–In–In–Se. Therefore, this configuration can be considered as two Se–In sublayers connected to each other by In–In bonding. Upon full fluorination, F atoms are discovered to energetically favorably adsorb on the top of In atoms.[27] However, the strong interaction between F and In atoms breaks the In–In bonds creating two isolated InSeF monolayers. When analysing the GaSe monolayer, R. Guo at el. discovered that the Ga–Ga bonds play the same role as the In–In bonds.[28] Upon full halogenation, isolated GaSeCl, GaSeBr, and GaSeI are formed by breaking Ga–Ga bonds.

In the current study, the full halogenation of InSe monolayers was performed with three different adsorption sites including the top of the In atom, the top of the Se atom, and the hollow position. It was found out that the configurations with halogen atoms vertically connected to the top of the In atom have the lowest total energies. Therefore, these configurations were used for further investigation. Upon full halogenation with Cl, Br and I atoms, the In–In bonds are also broken creating new isolated monolayers. As shown in Fig. 1(a), the top view of InSeX (X = Cl, Br, and I) monolayers reassembles into the honeycomb pattern like the pristine InSe monolayer. Meanwhile, the side view, as shown in Fig. 1(b), shows new monolayers consisting of sublayers in the order of Se–In–X (X = Cl, Br, and I).

The phonon dispersion calculation, shown in Fig. 1(c), confirms that the three new monolayers InSeCl, InSeBr, and InSeI are dynamically stable because of the lack of negative phonons in all three cases. For a monolayer, its cohesive energy is defined as the total energy required to separate it into individual atoms, divided by the total number of atoms in the unit cell.[35,50] The InSeX (X = Cl, Br and I) monolayers have 3 atoms per unit cell. Therefore, their cohesive energies E_{coh} are calculated as $E_{coh} = (E_{InSeX} - E_{In} - E_{Se} - E_X)/3$, where E_{InSeX}, E_{In}, E_{Se}, and E_X are the total energies of the InSeX monolayer and the systems of isolated In/Se/X atoms, respectively. The negative cohesive energies, as reported in Table 1, indicate that the three newly proposed monolayers are energetically stable.

The characteristics of optimized InSeX (X = Cl, Br, and I) monolayers and analogous 2D materials are reported in Table 1. Because the halogen atoms are adsorbed on the top of In atoms, they don't strongly affect the in-plane In–Se bonds or the lattice constants, leading to a small difference when comparing InSeX (X = Cl, Br, and I) monolayers to pristine InSe monolayers.[51] Similar results were also observed in halogenated GaSe monolayers; as reported in Table 1, the difference in lattice constants of GaSeCl, GaSeBr, and GaSeI is about 0.13 Å.[28] Meanwhile, the out-of-plane In–X bond lengths depend on the electronegativity of halogen atoms X. Cl atoms with higher electronegativity than Br and I form a shorter bond length, which is 2.32 Å compared to 2.48 Å and 2.65 Å for In–Br and In–I bond lengths, respectively. Being the most reactive among halogens, F forms the shortest bond length (2.23 Å) with In atoms. Moreover, the parent honeycomb phase changes into a 1T-like phase to allow one In atom to bond with two F atoms.[27]

Generally, Cl, Br and I are ideal to functionalize the surface of InSe monolayers because full halogenation with these elements results in isolated InSeX monolayers with a honeycomb pattern from the top view, Fig. 1(a), like the pristine InSe monolayer. Similar results were also observed for the GaSe monolayers, where the honeycomb phase is reserved after full halogenation with Cl, Br and I elements and the isolated GaSeX monolayers are also stable.[28]

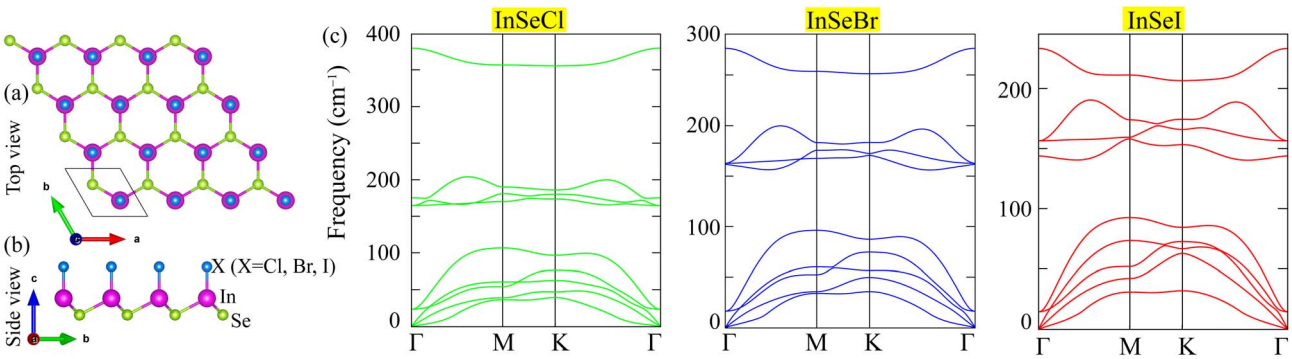

Fig. 1 (a) Top view, (b) side view and (c) phonon dispersion of monolayers InSeX (X = Cl, Br, and I).

Table 1 Structural characteristics of InSeX (X = Cl, Br and I) monolayers, including lattice constant a (Å), bond length d (Å, thickness of monolayers h (Å), cohesive energy E_{coh} (eV per atom), PBE/HSE06/PBE + SOC bandgap energies E_g (eV), work functions Φ (eV) on the halogen X (X = Cl, Br, and I) and Se surfaces, and the work function difference $\Delta\Phi$ (eV)

	a	d_{In-Se}	d_{In-X}	h	E_{coh}	E_g^{PBE}	E_g^{HSE06}	$E_g^{PBE+SOC}$	Φ_X	Φ_{Se}	$\Delta\Phi$
InSeCl	4.08	2.66	2.32	3.54	−3.34	1.91	2.94	1.82	7.80	6.00	1.18
InSeBr	4.09	2.66	2.48	3.69	−3.18	1.41	2.49	1.25	6.65	5.47	1.79
InSeI	4.15	2.69	2.65	3.86	−3.00	0.45	1.36	0.17	5.30	4.80	0.51

3.2 Electronic features of InSeX (X = Cl, Br, and I) monolayers

Indium selenide (InSe) monolayers, in both their pristine and doped forms, are promising for advanced sensor and optoelectronic applications, primarily due to their unique electronic structures.[27,52–54] Their electronic structures can be substantially altered through chemical doping or functionalization, leading to novel applications.[27,55,56] Consequently, a thorough understanding of the electronic structures and accurate prediction of the bandgaps of monolayers InSeX (X = Cl, Br, and I) are crucial for uncovering their properties and potential applications. To have a better insight into the structural properties of the three monolayers, their band structures were calculated along the Γ–K–M–Γ path, which connects the most symmetric $k-$ points in the Brillouin zone of the hexagonal structure. The calculations were performed using both the PBE and HSE06 approaches. While the PBE method generally provides correct qualitative features of the band structures,[33] the hybrid functional HSE06 yields more accurate band gaps.[57] This improved accuracy in the HSE06 approach originates from the partial inclusion of exact Hartree–Fock exchange in its exchange-correlation functional, which significantly lowers the self-interaction error (SIE) commonly found in standard DFT functionals like PBE.[58] All three halogenated InSe monolayers are direct bandgap semiconductors, with both the valence band maximum (VBM) and conduction band minimum (CBM) located at the $\Gamma-$ point. It is obvious that the introduction of Cl, Br, and I atoms effectively transforms the indirect bandgap of the pristine InSe monolayer[59] into direct bandgaps in halogenated configurations.

The PBE functional is known to systematically underestimate bandgaps because of the self-interaction error (SIE), which generally increases with the atomic number Z.[60] For indium-containing compounds (Z of In is 49), for example InN and InP, the bandgap difference between the PBE and HSE06 functionals is from 0.63 to 0.88 eV.[61,62] Similarly, Table 1 indicates that the HSE06 bandgap for pristine InSe is approximately 0.7 eV larger than the PBE result.[51,63] The spin–orbit coupling (SOC) effect is another important factor influencing the theoretical bandgap of both pristine and modified InSe monolayers. As shown by Liu *et al.*,[64] SOC can widen the bandgap in oxygen functionalized InSe monolayers by splitting the degenerate p_x and p_y orbitals. However, orbital splitting is often known to result in narrowing the bandgap when the VBM shifts upward and/or the CBM shifts downward.[65,66] As detailed in Table 1, applying the PBE + SOC method reduces the bandgaps of InSeX (X = Cl, Br, I) monolayers by 0.09 to 0.20 eV compared to the PBE method alone (Fig. 2). Consequently, the HSE06 method is more suitable for accurately predicting the bandgaps of these halogenated InSe monolayers.

The calculated HSE06 bandgaps are 2.94 eV for InSeCl, 2.49 eV for InSeBr, and 1.36 eV for InSeI. In the previous work of Yagmurcukardes,[27] the HSE06 bandgap of the InSeF monolayer is determined to be 3.01 eV. These results reveal a clear trend, where the bandgap of fully halogenated InSe monolayers is directly proportional to the electronegativity of the halogen atom. Furthermore, Fig. 2 highlights that the curvature of the band edges increases when moving down the halogen group. This increased curvature suggests a decrease in effective mass, which could lead to enhanced charge carrier mobility in these modified InSe monolayers, depending on the specific halogen atom.

It's evident that halogenation significantly alters the electronic structures of InSe monolayers. A deeper understanding of the halogen atoms' role in these changes can be obtained by analyzing the fat band structures (Fig. 3) and also eletrostatic potential (Fig. 4) of InSeX (X = Cl, Br, I) monolayers. In the pristine InSe monolayer, the buckled honeycomb structure arises from the sp^3 hybridization of In-5s and In-5p orbitals.[67,68]

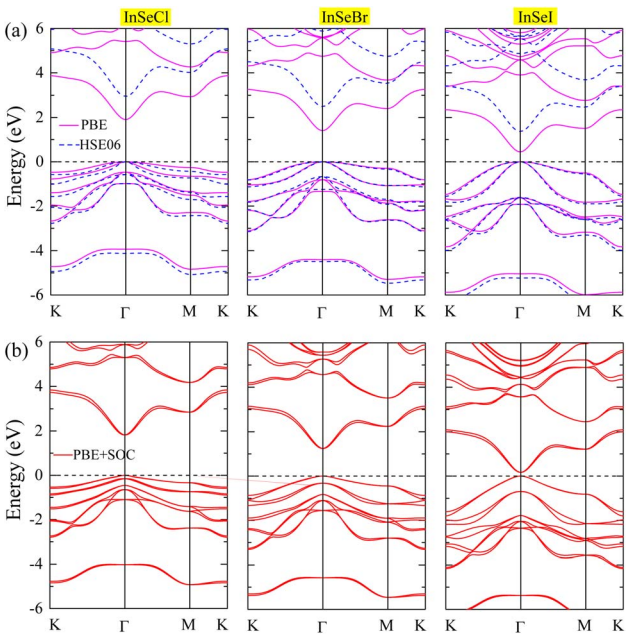

Fig. 2 Electronic band structures of InSeX monolayers (X = Cl, Br, I) calculated using (a) PBE method (solid pink lines), HSE06 method (blue dashed lines), and (b) PBE + SOC method (solid red lines).

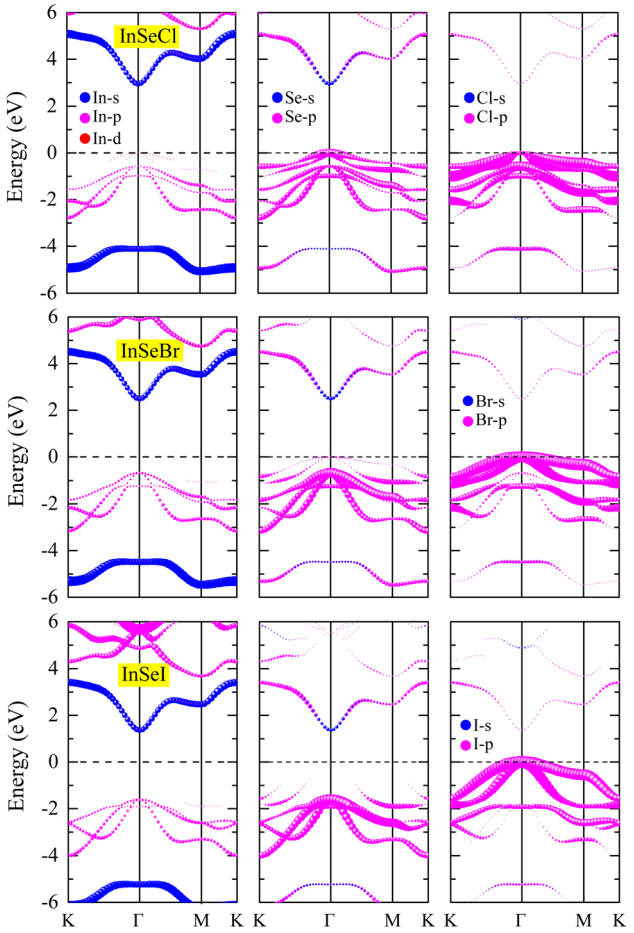

Fig. 3 Fat band of InSeX (X = Cl, Br, I) monolayers.

Each In atom forms bonds with three Se atoms through the overlap of In-sp^3 and Se-4p orbitals. One remaining In-sp^3 orbital on each In atom forms a covalent In–In bond, which connects the lower Se–In sublayer with the upper In–Se sublayer. As a result, the band structure of the pristine InSe monolayer[67] is characterized by well-hybridized In-s, In-p, and Se-p orbitals occupying a wide energy range, from −4 to −2 eV in the valence bands and the lower conduction bands.

Due to full halogenation, the In–In bonds are broken because the In-sp^3 hybrid orbitals disappear. As depicted in Fig. 3, the In-5s orbitals become highly localized in the −5 to −4 eV region of the valence band and also dominate the lowest conduction band. In contrast, the In-5p orbitals primarily occupy the energy range from −3 to −0.7 eV. The absence of In-sp^3 orbitals results in the formation of isolated InSeX (X = Cl, Br, I) monolayers, which are stabilized by the hybridization of In-5p, Se-4p, and X-p orbitals in the energy levels ranging from −3 to −0.7 eV. These halogenated monolayers retain buckled honeycomb structures, which are now supported by new sp^3 hybridization involving Se orbitals, as indicated by the mix of Se-4s (blue) and Se-4p (pink) orbitals near −4 eV in the valence band. The VBM is mainly composed of Se-4p and X-p orbitals, leading to a significant bandgap change depending on the halogen atoms. The strong contribution of X-p orbitals near the VBM also causes a shift of the VBM to the Γ − point. Meanwhile, the CBM remains at the Γ − point since the halogen atoms contribute little to the lowest conduction bands. Consequently, the fully halogenated InSe monolayers exhibit direct bandgaps, with both the VBM and CBM located at the Γ − point.

As one moves down the halogen group from Cl to Br and I, the atomic radius increases, resulting in a longer In–X bond length (as reported in Table 1) and a greater separation between Se and X atoms. This increased spacing causes the X-p and Se-4p orbital hybridization to occur at lower energy levels in the valence band, as shown in Fig. 3. As a result, the valence band near the Fermi level becomes increasingly dominated by X-p orbitals, leading to a gradual reduction in the bandgap. Despite these significant changes in bandgap values, the geometry of the fully halogenated InSe monolayers is preserved. The bonding remains stabilized by hybridized In-5s/5p, Se-4p, and X-p orbitals, and the In–Se bond lengths remain nearly unchanged across all three compositions (as shown in Table 1). Furthermore, the monolayer structures remain nearly perfectly symmetric, as confirmed by the direction-independent values of Young's modulus and Poisson's ratio presented in Fig. 5.

InSe monolayers have been widely studied and shown to be promising candidates for gas sensing applications, where their work function (denoted as Φ) plays an important role in selective sensitivity. For example, Ni-doped InSe monolayers can be

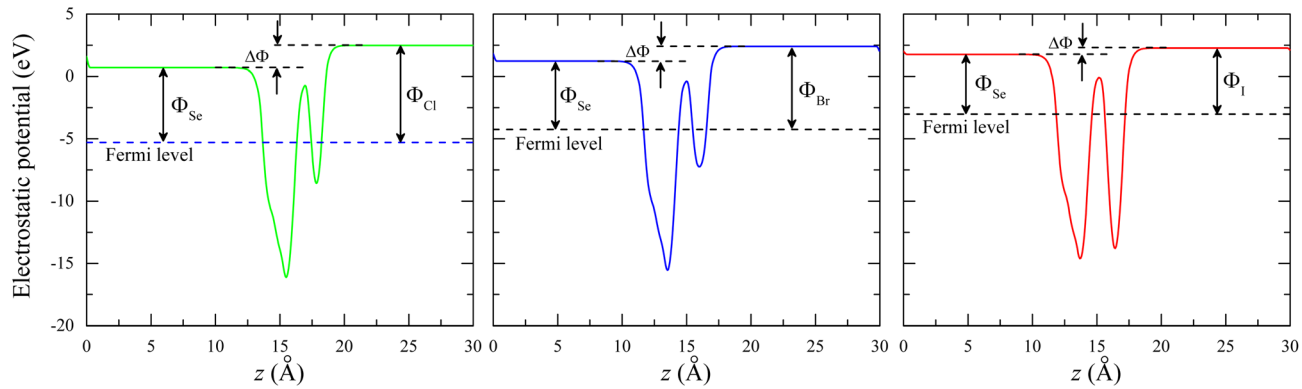

Fig. 4 Electrostatic potential of InSeX (X = Cl, Br, I) monolayers as a function of distance in the z − direction. Φ_{Se} and Φ_X represent the work functions on the Se and X (X = Cl, Br, or I) surfaces, respectively, with $\delta\Phi$ indicating the difference between these two work functions.

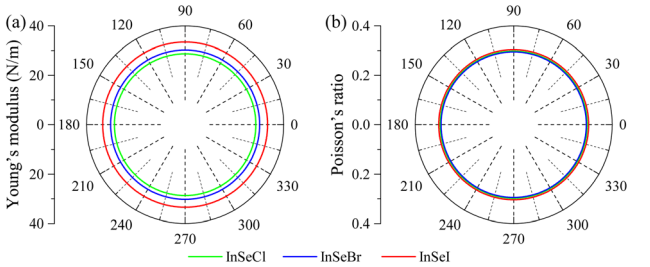

Fig. 5 (a) Young's modulus $Y(\beta)$ and (b) Poisson's ratio $\nu(\beta)$ as functions of in-plane angle β in InSeX (X = Cl, Br, and I) monolayers.

used as effective Φ − type gas sensors for SO_2, NH_3, and CO due to significant work function changes upon gas adsorption – ranging from 6.67% to 11.29%.[12] Similarly, by analyzing the rate of work function variation, InSe monolayers doped with Pd, Pt, Rh, Ru, and Cu have been theoretically identified as promising Φ − type sensors for detecting gases such as NH_3, SO_2, CO, NO, and NO_2.[53,69,70]

As shown in Fig. 1, the halogenated InSeX (X = Cl, Br, I) monolayers have out-of-plane asymmetry, analogous to Janus monolayers with different atoms on each surface. This structural asymmetry generates an intrinsic vertical dipole, or a permanent out-of-plane electric field, across the monolayer.[71,72] As a result, these monolayers are expected to exhibit different work functions on their top and bottom surfaces. Fig. 4 displays the variation in electrostatic potentials for the three monolayers, where dashed lines indicate the Fermi level (E_{Fermi}) and solid horizontal lines represent the vacuum level (E_{vac}). The work function Φ is defined as the minimum energy required to remove an electron from the Fermi level to a point immediately outside the surface in a vacuum and is given by the relation $\Phi = E_{vac} - E_{Fermi}$. As reported in Table 1, the work functions on the Se-terminated surfaces (Φ_{Se}) range from 4.80 to 6.00 eV. Compared with the pristine InSe monolayer ($\Phi_{pristine} = 5.70$ eV) and the fully fluorinated InSeF monolayer ($\Phi = 6.28$ eV),[27] it is evident that halogenation effectively modifies the work function of InSe monolayers. Moreover, halogens with higher electronegativity tend to induce larger work function values. The work functions on the halogen-terminated surfaces (Φ_X, where X = Cl, Br, I) range from 5.30 to 7.80 eV, which are 0.51–1.79 eV higher than the corresponding Φ_{Se}. This vertical asymmetry in the electronic structure of InSeX monolayers offers potential advantages for many applications.

In the context of gas sensing, 2D materials with intrinsic dipoles may present an electron-rich surface on one side, promoting strong adsorption of electron-accepting gases, while the opposite side remains less reactive or even repulsive to the same species.[73,74] In field-effect transistor (FET) applications, this asymmetry allows the possibility of fabricating both n-type and p-type transistors from the same material by contacting opposite surfaces without the need for extrinsic doping.[75] Experimental studies on Janus MoSSe have demonstrated that the difference in the work function between its two surfaces leads to distinct contact band alignments, altering Fermi level pinning and even transforming a Schottky contact into an ohmic one under bias.[76] Overall, full halogenation using different Group XVII elements offers a straightforward strategy to modulate the work function of InSe monolayers. The Cl and Br atoms, due to their higher electronegativities, increase the work function, while I, having less electronegativity, reduces the work function. The magnitude of work function deviation can thus be tuned by selecting the appropriate halogen atom. Consequently, InSeX (X = Cl, Br, I) monolayers with appropriate work functions can be chosen for applications such as highly sensitive and selective chemoresistive sensors, high-performance FETs, and vertically polarized electronic devices.

3.3 Elastic and piezoelectric features of InSeX (X = Cl, Br, I) monolayers

Piezoelectric applications, including actuators, sensors, and energy harvesting systems, fundamentally rely on non-centrosymmetric materials that generate polarization charges in response to external mechanical stress.[77,78] With the increasing need for small-scale and diverse-functional devices, two-dimensional (2D) piezoelectric nanomaterials have emerged as highly promising candidates. Their ultrathin nature, superior electromechanical coupling, and other distinct physical attributes make them exceptionally intriguing.[79] Thus, a comprehensive investigation into the elastic and piezoelectric characteristics of InSeX (X = Cl, Br, and I) monolayers is warranted.

To estimate the mechanical stability of InSeX (X = Cl, Br, and I) monolayers, their elastic constants C_{11}, C_{12}, and C_{66} were calculated using the general formula:

$$C_{ij} = \frac{1}{A_0} \times \frac{\partial^2 E(\varepsilon)}{\partial \varepsilon_i \partial \varepsilon_j} \quad (1)$$

where A_0 is the area of the unit cell and $E(\varepsilon)$ is the energy-strain function derived by fitting total energy values to corresponding strain rates from a series of slightly deformed configurations. The Young's modulus Y_{2D} and Poisson's ratio ν were calculated based on elastic constants C_{11} and C_{12} as follows:

$$Y_{2D} = \frac{{C_{11}}^2 - {C_{12}}^2}{C_{11}} \quad (2)$$

$$\upsilon = \frac{C_{12}}{C_{11}} \quad (3)$$

As reported in Table 2, the elastic constant C_{11} is positive and it is also higher than C_{12}, confirming the mechanical stability of InSeX (X = Cl, Br, and I) monolayers according to Born's criteria.[80,81] The Young's moduli of the three monolayers are in the range of 28.69–33.44 N m^{-1}, which are comparable to those of materials with closely similar configurations such as 2D GaXY (X = S, Se; Y = F, Cl, Br, I) 37.11–49.75 N m^{-1}.[28,82] The low Young's moduli make these monolayers exceptionally flexible compared to stiffer materials like graphene, MoS_2 and h-BN monolayers.[83–85] The Poisson's ratios of the three monolayers InSeX (X = Cl, Br, and I) are very close to each other; after rounding to 2 significant figures, they are all equal to 0.3. This

Table 2 The elastic coefficients (C_{11}, C_{12}, and C_{66}), Young's modulus Y_{2D}, Poisson's ratio ν and piezoelectric coefficients e_{11}, e_{31}, d_{11} and d_{31} of InSeX (X = Cl, Br, and I) monolayers

	C_{11}	C_{12}	C_{66}	Y_{2D}	ν	e_{11}	e_{31}	d_{11}	d_{31}
	N m^{-1}	N m^{-1}	N m^{-1}	N m^{-1}		10^{-10} C m^{-1}	10^{-10} C m^{-1}	(pm V^{-1})	(pm V^{-1})
InSeCl	31.50	9.38	11.05	28.69	0.30	5.60	0.02	33.50	0.86
InSeBr	33.18	9.88	11.65	30.24	0.30	3.68	0.10	19.10	0.54
InSeI	36.77	11.07	12.85	33.44	0.30	3.34	0.61	14.90	0.21

value is slightly higher than that of pristine InSe monolayers and halogenated GaSeX (X = Cl, Br, and I) monolayers.[24,28] It is worth noting that 2D materials with a Poisson's ratio of approximately 0.3 – such as graphene, MoS_2, and h-BN[86–88] – are considered to have a "conventional" mechanical response. This value is typical for many isotropic solids and indicates a balance between stiffness and flexibility.[89] A Poisson's ratio of 0.3 suggests a good compromise between rigidity and ductility, making these materials less prone to brittle failure compared to auxetic (negative Poisson's ratio) materials.[90] Due to the balance between lateral and axial strains, such materials maintain adhesion and structural integrity under bending and stretching, making them more compatible with a wide range of substrates in flexible electronics, reducing delamination risks.[91]

To identify the elastic isotropy of monolayers InSeX (X = Cl, Br, and I), it is necessary to determine the dependence of Young's modulus and Poisson's ratio on the in-plane angle β. In further discussion, the Young's modulus and Poisson's ratio functions are denoted as $Y_{2D}(\beta)$ and $\nu(\beta)$, respectively. The angular functions $Y_{2D}(\beta)$ and $\nu(\beta)$ can be calculated using elastic constants C_{11}, C_{12}, and C_{66} as follows:[92,93]

$$Y_{2D}(\beta) = \frac{C_{11}C_{22} - C_{12}^2}{C_{11}\sin^4\beta + C_{22}\cos^4\beta + \left(\frac{C_{11}C_{22} - C_{12}^2}{C_{66}} - 2C_{12}\right)\sin^2\beta\cos^2\beta} \quad (4)$$

$$\nu(\beta) = \frac{C_{12}\left(\sin^4\beta + \cos^4\beta\right) - \left(C_{11} + C_{22} - \frac{C_{11}C_{22} - C_{12}^2}{C_{66}}\right)\sin^2\beta\cos^2\beta}{C_{11}\sin^4\beta + C_{22}\cos^4\beta - \left(2C_{12} - \frac{C_{11}C_{22} - C_{12}^2}{C_{66}}\right)\sin^2\beta\cos^2\beta} \quad (5)$$

The calculated angular functions $Y_{2D}(\beta)$ and $\nu(\beta)$ are plotted in Fig. 5, respectively. In all three monolayers, the $Y_{2D}(\beta)$ and $\nu(\beta)$ lines are nearly perfect circles indicating the highly isotropic elasticity. This result makes InSeX (X = Cl, Br, and I) monolayers very special cases compared to pristine InSe or fluorinated InSeF monolayers[27] whose Young's modulus and Poisson's ratios depend on the orientation of the applied strains.

In general, our isotropic 2D materials with an in-plane Young's modulus of about 30 N m^{-1} and Poisson's ratio of 0.3 deliver an exceptional flexibility and mechanical stability, making them highly suitable for stretchable electronics, wearable sensors, and conformal coatings. Their relatively low stiffness enables large-strain accommodation and reduces stress concentrations compared to graphene (Y = 340 N m^{-1} and $\nu = 0.17$)[94] or rigid transition-metal dichalcogenides such as monolayer MoS_2 ($Y = 180 \pm 60$ N m^{-1} and $\nu = 0.29$),[95] both of which despite their outstanding strength can suffer from limited bendability and more pronounced anisotropic behavior. Furthermore, the moderate Poisson's ratio of 0.3 ensures predictable, uniform lateral contraction under tension, avoiding the design complexities of auxetic materials (such as borophene) while still enabling effective strain-induced band-structure tuning. By combining mechanical compliance with isotropic elastic response, these materials offer a versatile platform for resilient, high-performance devices that must endure repeated flexing and large deformations without mechanical failure.

Using the VASP package, piezoelectric coefficients are calculated using the modern theory of polarization,[96–98] which is based on the Berry phase formalism. This method enables the determination of the polarization vector Pi as a function of the second-rank strain e_{jk} and stress σ_{jk} tensors. Once the polarization Pi is obtained, the third-rank piezoelectric tensors e_{ijk} and d_{ijk} can be derived accordingly.[99]

$$e_{ijk} = \frac{\partial P_i}{\partial \varepsilon_{jk}} \quad (6)$$

$$d_{ijk} = \frac{\partial P_i}{\sigma_{jk}} \quad (7)$$

where $i, j, k \subset (1,2,3)$, corresponding to the Cartesian directions x, y and z, respectively. The piezoelectric tensors e_{ijk} and d_{ijk} can be simplified by symmetric analysis allowing the determination of piezoelectric coefficients $d_{11} = e_{11}/(C_{11} - C_{12})$ and $d_{31} = e_{31}/(C_{11} + C_{12})$.[100,101] The e_{11} and e_{31} coefficients can be determined by evaluating the change of in-plane polarization and out-of-plane polarization[102,103] as uniaxial strains are applied to the supercells of InSeX (X = Cl, Br, and I) monolayers. Because the pristine InSe monolayer belongs to D_{3h} point group symmetry, its non-zero piezoelectric coefficients are e_{11} and d_{11}.[99] Upon full halogenation, the InSeX (X = Cl, Br and I) monolayers become slightly distorted, breaking the vertical mirror symmetry.

Consequently, these monolayers also exhibit out-of-plane piezoelectric coefficients e_{31} and d_{31}. Reference data of the clamped-ion piezoelectric coefficients of InSeX (X = Cl, Br, and I) monolayers are reported in Table 2.

As reported in Table 2, the InSeX (X = Cl, Br and I) monolayers are strongly piezoelectric with e_{11} in the range of 3.34–5.60 × 10^{-10} C m^{-1} and d_{11} of 14.90–33.50 pm V^{-1}. Such piezoelectricity is in the same order as that of well-known 2D piezoelectric materials such as GaS, h-BN, and MoS_2 (ref. 99 and 104) and significantly higher than those of many transition-metal dichalcogenides (MX_2, where M = Mo, W and X = S, Se, Te).[99,105] A general trend is also observed that piezoelectric response increases with the electronegativity of the halogen atom. In particular, due to chlorine's high electronegativity, the InSeCl monolayer exhibits even greater in-plane piezoelectricity than pristine InSe.[104] This strong piezoelectric behavior highlights the potential of InSeX monolayers for applications in energy harvesting, pressure/strain sensing, and photodetection. For instance, Wu *et al.* demonstrated a monolayer MoS_2 nanogenerator capable of harvesting mechanical energy.[106] Similarly, a monolayer WSe_2-based piezoelectric nanogenerator achieved a peak output voltage of 45 mV under 0.39% strain.[107] InSe monolayers have been employed as the active layer in flexible field-effect transistor (FET)-based pressure sensors, capable of detecting a minimum load of 0.1 g, producing an output of 0.2 mV.[108] Furthermore, multilayer γ-InSe has been integrated into high-performance, self-powered flexible photodetectors, delivering an impressive photon responsivity of 824 mA W^{-1} under 400 nm illumination at 0.368 mW cm^{-2}.[109]

In summary, the combination of strong in-plane piezoelectricity, the presence of out-of-plane components, and intrinsic mechanical flexibility makes InSeX (X = Cl, Br, and I) monolayers promising candidates for self-powered nanosensors, nanogenerators, and flexible optoelectronic devices.

3.4 Optical properties of InSeX (X = Cl, Br and I) monolayers

Two-dimensional (2D) semiconductors with tunable bandgaps, band edge positions, and work functions have emerged as promising photocatalysts for water splitting and solar energy conversion.[110–112] By adjusting their composition and thickness, or forming van der Waals heterostructures, these materials can be engineered to absorb a broad range of sunlight while aligning their band edges with the redox potentials of water.[113,114] In particular, monolayer indium selenide (InSe) combines excellent charge mobility with a valence band position more positive than the water oxidation potential, and its tunable bandgap (down to about 1.2 eV) enables strong visible-light absorption.[17] Therefore, the optical properties of InSeX (X = Cl, Br and I) were calculated and presented in Fig. 6.

As shown in Fig. 6(a), the real part of the dielectric function, $\varepsilon_1(\omega)$, remains positive across the examined photon energy range for all InSeX (X = Cl, Br, I) monolayers, indicating transparency and the ability to sustain propagating optical modes without metallic screening effects in this range. Variations in ε_1 reflect differences in refractive index dispersion, with InSeI generally exhibiting higher values, suggesting stronger

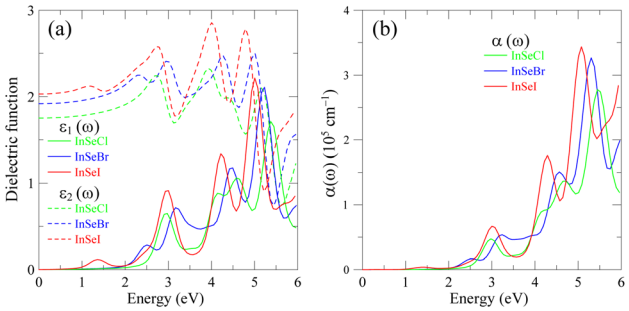

Fig. 6 Dielectric functions (a) and absorption rate (b) of InSeX (X = Cl, Br and I) monolayers calculated by the HSE06 method.

light–matter interaction. The imaginary part, $\varepsilon_2(\omega)$, shows pronounced peaks between 2 and 5 eV, corresponding to interband electronic transitions that dominate optical absorption. The lower onset of $\varepsilon_1(\omega)$ in InSeI indicates a narrower optical bandgap compared to InSeCl and InSeBr, implying that InSeI can absorb lower-energy photons, which may enhance its utility in visible-light-driven optoelectronic and photocatalytic applications.

The absorption spectra $\alpha(\omega)$ of the InSeX (X = Cl, Br, I) monolayers reveal distinct onset energies and intensity profiles, indicating differences in optical bandgaps and photon-harvesting capabilities. InSeI exhibits the lowest absorption onset (about 2.5 eV), confirming its narrower bandgap and enabling it to absorb a broader portion of the visible spectrum compared to InSeCl and InSeBr. All three monolayers display strong absorption peaks, $\alpha(\omega)$ above 10^5 cm^{-1}, for photons with energy higher than 4 eV, corresponding to interband transitions in the near-UV region, with InSeI showing the highest peak intensity, suggesting enhanced light–matter interaction. These properties make InSeI particularly promising for visible-light-driven optoelectronic applications, while all three materials could be useful in UV photodetectors, photocatalysis, and high-efficiency solar energy conversion devices, where strong and tunable absorption is essential.

3.5 Transport properties

Although the PBE functional typically underestimates semiconductor band gaps, this has only a limited effect on mobility calculations, as errors in the band gap and velocity matrix elements can partially cancel out each other.[115] In practice, the PBE functional often reproduces band dispersion and effective masses with sufficient accuracy to yield mobilities close to experimental values.[116] More advanced approaches, such as hybrid functionals or GW, can refine band energies and effective masses, but their significantly higher computational cost is rarely justified for mobility-focused studies. As a result, the PBE method was used to investigate the transport properties of InSeX (X = Cl, Br and I) monolayers, which offers a practical compromise between accuracy and efficiency. Similar to other 2D materials with asymmetric electronic structures,[117,118] the intrinsic out-of-plane dipole present in InSeX (X = Cl, Br, and I) monolayers is expected to be an internal driving force when the

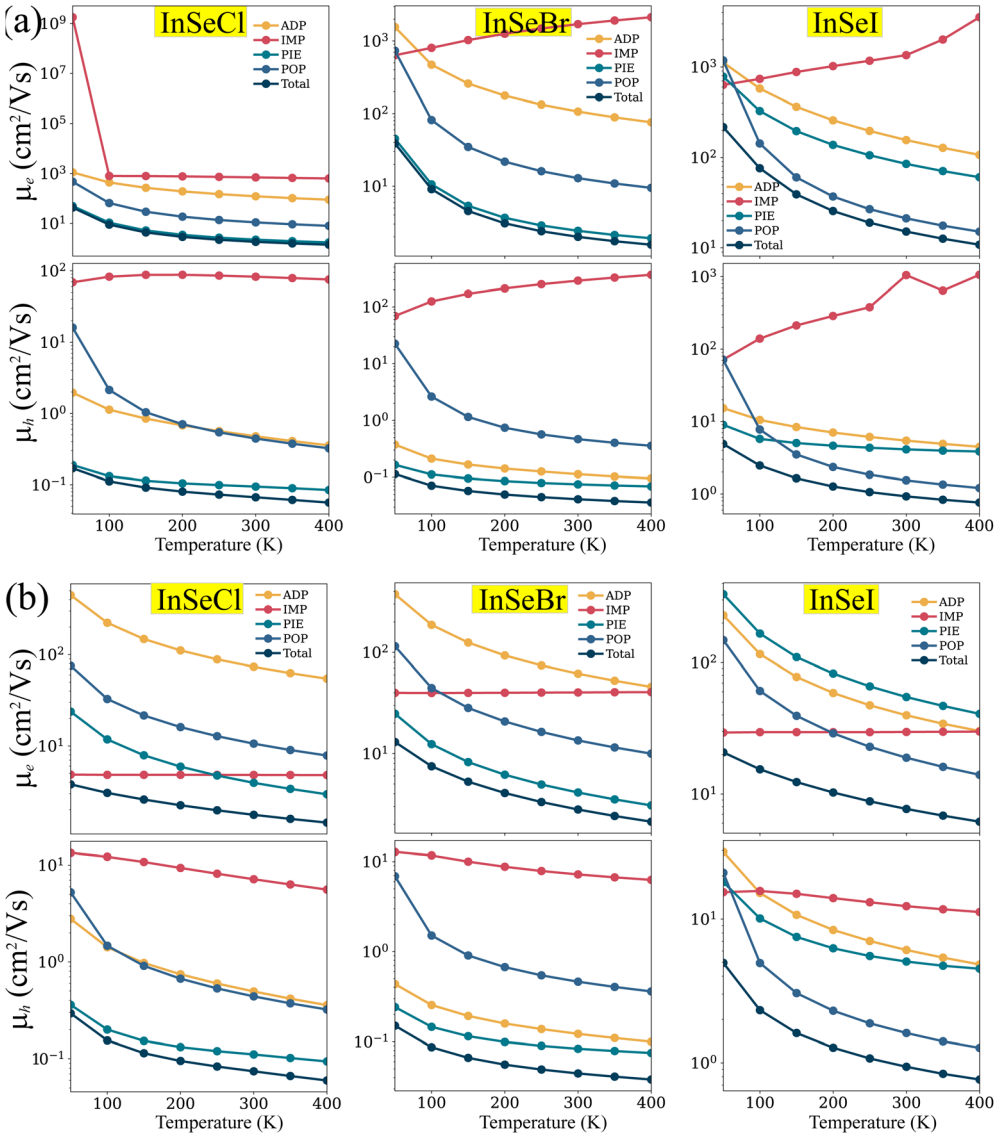

Fig. 7 Temperature-dependence of electron μ_e and hole μ_h mobilities as functions of temperature for InSeX monolayers (X = Cl, Br, I) at carrier concentrations of (a) 1×10^{16} cm^{-3} and (b) 1×10^{20} cm^{-3}.

materials are under illumination, shifting electrons toward the lower-potential surface and holes toward the higher-potential surface. This built-in electric field can work as an atomic-scale p–n junction,[117] enhancing the separation of photogenerated carriers and suppressing recombination. As a result, understanding the charge transport behavior of these isolated monolayers is of particular interest. To explore this, charge carrier mobilities were calculated while accounting for several critical factors including carrier concentrations at 10^{16} cm^{-3} and 10^{20} cm^{-3}, temperature ranging from 50 K to 400 K, and four primary scattering mechanisms – acoustic deformation potential μ_{ADP}, ionized impurity μ_{IMP}, piezoelectric μ_{PIE}, and polar optical phonon μ_{POP} scatterings. At each temperature and carrier density, the total carrier mobility μ_{TOT} was computed using Matthiessen's rule:[48,119]

$$\frac{1}{\mu_{TOT}} = \frac{1}{\mu_{ADP}} + \frac{1}{\mu_{IMP}} + \frac{1}{\mu_{PIE}} + \frac{1}{\mu_{POP}} \quad (8)$$

For the InSeCl monolayer at 50 K, the total electron mobility at low carrier concentrations is 43.11 cm^2 V^{-1} s^{-1}, which is ten times higher than that at high concentrations. In contrast, hole mobility increases slightly from 0.17 to 0.29 cm^2 V^{-1} s^{-1} with an increasing carrier concentration. As temperature increases to 400 K, the total electron mobilities for both carrier densities converge to ~1.40 cm^2 V^{-1} s^{-1}. A similar trend is observed in hole mobilities, which decline and stabilize near 0.06 cm^2 V^{-1} s^{-1} regardless of doping. In the case of InSeBr, the impact of carrier concentration is less pronounced. At 50 K, electron mobilities are 38.91 cm^2 V^{-1} s^{-1} at low concentrations and 13.03 cm^2 V^{-1} s^{-1} at high concentrations, while hole mobilities differ by only 0.04 cm^2 V^{-1} s^{-1}. As temperature increases to 400

K, electron mobility reduces to 1.56 $cm^2 V^{-1} s^{-1}$ (low concentration) and 2.12 $cm^2 V^{-1} s^{-1}$ (high concentration), and hole mobilities become nearly insensitive to carrier concentration at higher temperatures. InSeI shows particularly promising transport performance. At 50 K, the electron mobility reaches 217.33 $cm^2 V^{-1} s^{-1}$, remaining relatively high (10.82 $cm^2 V^{-1} s^{-1}$) even at 400 K. However, mobility drops sharply at high carrier concentrations. Hole mobilities in InSeI are nearly independent of carrier density. At both carrier concentrations of 10^{16} cm^{-3} and 10^{20} cm^{-3}, the hole mobilities are between 4.89 and 4.95 $cm^2 V^{-1} s^{-1}$ at 50 K, decreasing to ~0.76 $cm^2 V^{-1} s^{-1}$ as temperature increases to 400 K.

Generally, higher temperature enhances the phonon activity and all scattering mechanisms, resulting in reduced charge carrier mobility. As shown in Fig. 7, the PIE scattering dominates mobility degradation in InSeCl and InSeBr, but has a significantly reduced impact on InSeI, allowing the InSeI monolayer to retain relatively high electron mobility. PIE scattering originates from internal electric fields induced by lattice strain under acoustic phonons, particularly in non-centrosymmetric materials.[120] All three halogenated monolayers (InSeCl, InSeBr, and InSeI) lack inversion symmetry and are thus subject to PIE scattering. However, the magnitude of this effect depends inversely on the stiffness of the lattice. A stiffer lattice, characterized by a higher Young's modulus, deforms less under phonons and thereby reduces the strength of the piezoelectric field.[121] InSeI, with the highest Young's modulus among the three (as reported in Table 1 and Fig. 5(a), therefore, experiences the weakest PIE scattering contribution to mobility degradation.

Prior studies on pristine InSe monolayers have shown that mobility is strongly influenced by dimensionality and scattering effects. At 300 K, electron mobility decreases from 1060 $cm^2 V^{-1} s^{-1}$ in bulk to 220 $cm^2 V^{-1} s^{-1}$ in the bilayer and 120 $cm^2 V^{-1} s^{-1}$ in the monolayer. Similarly, hole mobility drops from 21 $cm^2 V^{-1} s^{-1}$ in the bulk to 3 and 0.5 $cm^2 V^{-1} s^{-1}$ in the bilayer and monolayer, respectively.[122] Furthermore, including the POP scattering reduces both electron and hole mobilities by an order of magnitude at room temperature.[123,124] The relatively low mobilities observed in halogenated InSeX (X = Cl, Br, I) monolayers may be attributed to their reduced number of sublayers – each monolayer comprises an In–Se–X structure compared to the Se–In–In–Se stacking in pristine InSe. Moreover, introducing all four scattering mechanisms (ADP, IMP, PIE, and POP) significantly lowers the total mobility. Despite this reduction, the inclusion of these mechanisms provides a comprehensive and realistic understanding of carrier transport in these functionalized 2D materials, which is essential for evaluating their potential in electronic and optoelectronic applications.

4 Conclusion

In this study, first-principles calculations were carried out to investigate the mechanism of forming isolated InSeX (X = Cl, Br, and I) monolayers from pristine InSe monolayers through full halogenation. The moderate electronegativities of Cl, Br, and I allow the formation of energetically and dynamically stable Se–In–X stacking configurations. Upon halogenation, the In-sp^3 hybrid orbitals disappear, leading to the breaking of In–In bonds in the Se–In–In–Se monolayer. At the same time, isolated Se–In–X configurations are formed and their buckled honeycomb geometry is preserved by the emerging Se-sp^3 hybrid orbitals. The electronic parameters of InSe monolayers can be effectively modified by halogenation with different elements. A general trend was found out that the bandgap and work function decrease gradually when moving down the halogen group from Cl to Br and I. Moreover, the higher Young's modulus leads to significantly higher charge carrier mobility because a stiffer monolayer lowers the PIE scattering mechanism, which is the most dominant in monolayers with a lack of inversion symmetry like InSeX (X = Cl, Br, and I) monolayers. The significant difference in the work functions on the Se-surface and X-surface make it possible for the InSeX (X = Cl, Br, and I) monolayers to be of great potential for application in selective and sensitive Φ-type gas sensors. With a wide range of variation in the bandgap, band edge and work function, these monolayers are promising subjects for studies relating to photocatalytic water splitting and solar energy conversion. Due to the significant piezoelectric coefficients and high tunable light absorption rate, these fully halogenated monolayers are also promising for applications in energy harvesting, pressure/strain sensors and photodetectors. Finally, the stable buckled honeycomb InSeX (X = Cl, Br, and I) monolayers belong to a new 2D family which can be expanded by applying the same procedure for group-XIII monochalcogenides MX (M = B, Al, Ga, In, Tl and X = S, Se, Te) in future studies.

Conflicts of interest

There are no conflicts of interest to declare.

Data availability

All data that support the findings of this study are included within the article.

References

1 S. Sucharitakul, N. J. Goble, U. R. Kumar, R. Sankar, Z. A. Bogorad, F.-C. Chou, Y.-T. Chen and X. P. Gao, *Nano Lett.*, 2015, **15**, 3815–3819.
2 G. W. Mudd, S. A. Svatek, T. Ren, A. Patanè, O. Makarovsky, L. Eaves, P. H. Beton, Z. D. Kovalyuk, G. V. Lashkarev, Z. R. Kudrynskyi, *et al.*, *Adv. Mater.:Compos. Carbon, Pap. Symp.*, 2013, **25**, 5714.
3 H.-C. Chang, C.-L. Tu, K.-I. Lin, J. Pu, T. Takenobu, C.-N. Hsiao and C.-H. Chen, *Small*, 2018, **14**, 1802351.
4 C.-H. Wu, Y.-C. Huang, Y.-T. Ho, S.-J. Chang, S.-K. Wu, C.-H. Huang, W.-C. Chou and C.-S. Yang, *Nanomaterials*, 2022, **12**, 2435.
5 S. Song, S. Jeon, M. Rahaman, J. Lynch, D. Rhee, P. Kumar, S. Chakravarthi, G. Kim, X. Du, E. W. Blanton, *et al.*, *Matter*, 2023, **6**, 3483–3498.

6 D. A. Bandurin, A. V. Tyurnina, G. L. Yu, A. Mishchenko, V. Zólyomi, S. V. Morozov, R. K. Kumar, R. V. Gorbachev, Z. R. Kudrynskyi, S. Pezzini, *et al.*, *Nat. Nanotechnol.*, 2017, **12**, 223–227.
7 S. Lei, L. Ge, S. Najmaei, A. George, R. Kappera, J. Lou, M. Chhowalla, H. Yamaguchi, G. Gupta, R. Vajtai, *et al.*, *ACS Nano*, 2014, **8**, 1263–1272.
8 M. Li, C.-Y. Lin, S.-H. Yang, Y.-M. Chang, J.-K. Chang, F.-S. Yang, C. Zhong, W.-B. Jian, C.-H. Lien, C.-H. Ho, *et al.*, *Adv. Mater.*, 2018, **30**, 1803690.
9 W. Feng, W. Zheng, W. Cao and P. Hu, *Adv. Mater.*, 2014, **26**, 6587–6593.
10 H. Jin, J. Li, Y. Dai and Y. Wei, *Phys. Chem. Chem. Phys.*, 2017, **19**, 4855–4860.
11 S. R. Tamalampudi, Y.-Y. Lu, R. K. U, R. Sankar, C.-D. Liao, C.-H. Cheng, F. C. Chou and Y.-T. Chen, *Nano Lett.*, 2014, **14**, 2800–2806.
12 J. Dong, X. Qiu, S. Huang, S. Lin, L. Liu and H. Xiong, *Chemosensors*, 2024, **12**, 219.
13 Y. Cai, G. Zhang and Y.-W. Zhang, *J. Phys. Chem. C*, 2017, **121**, 10182–10193.
14 L. Zhang, Z. Li, J. Liu, Z. Peng, J. Zhou, H. Zhang and Y. Li, *Anal. Chem.*, 2020, **92**, 11277–11287.
15 M. A. Kishore and P. Ravindran, *AIP Conf. Proc.*, 2017, 090029.
16 Q. Peng, R. Xiong, B. Sa, J. Zhou, C. Wen, B. Wu, M. Anpo and Z. Sun, *Catal. Sci. Technol.*, 2017, **7**, 2744–2752.
17 H. Zheng, Y. Lu, K.-H. Ye, J. Hu, S. Liu, J. Yan, Y. Ye, Y. Guo, Z. Lin, J. Cheng, *et al.*, *Nat. Commun.*, 2021, **12**, 91.
18 Z. Ma, R. Li, R. Xiong, Y. Zhang, C. Xu, C. Wen and B. Sa, *Materials*, 2021, **14**, 3768.
19 N. T. Han, J. Guerrero-Sanchez and D. Hoat, *Nanoscale Adv.*, 2025, **7**, 1443–1451.
20 F. Ersan, H. Arkin and E. Aktürk, *RSC Adv.*, 2017, **7**, 37815–37822.
21 H. Arkın and E. Aktürk, *Appl. Surf. Sci.*, 2016, **390**, 185–189.
22 I. Ozdemir, H. Ozaydin, H. Arkin and E. Aktürk, *Mater. Res. Express*, 2019, **6**, 065032.
23 Y. Kadioglu, F. Ersan, D. Kecik, O. Ü. Aktürk, E. Aktürk and S. Ciraci, *Phys. Chem. Chem. Phys.*, 2018, **20**, 16077–16091.
24 T. Hu, J. Zhou and J. Dong, *Phys. Chem. Chem. Phys.*, 2017, **19**, 21722–21728.
25 H. Guo, Y. Yin, W. Yu, J. Robertson, S. Liu, Z. Zhang and Y. Guo, *Nanoscale*, 2023, **15**, 3496–3503.
26 Q. Hao, J. Liu, G. Wang, J. Chen, H. Gan, J. Zhu, Y. Ke, Y. Chai, J. Lin and W. Zhang, *ACS Nano*, 2020, **14**, 11373–11382.
27 M. Yagmurcukardes, *Phys. Rev. B*, 2019, **100**, 024108.
28 R. Guo, R. Zhao, Y. Ge, Y. Liu and W. Wan, *Appl. Phys. Lett.*, 2023, **123**, 063102.
29 G. Kresse and J. Furthmüller, *Phys. Rev. B:Condens. Matter Mater. Phys.*, 1996, **54**, 11169–11186.
30 G. Kresse and J. Furthmüller, *Comput. Mater. Sci.*, 1996, **6**, 15–50.
31 P. E. Blöchl, *Phys. Rev. B:Condens. Matter Mater. Phys.*, 1994, **50**, 17953.
32 G. Kresse and D. Joubert, *Phys. Rev. B:Condens. Matter Mater. Phys.*, 1999, **59**, 1758–1775.
33 J. P. Perdew, K. Burke and M. Ernzerhof, *Phys. Rev. Lett.*, 1996, **77**, 3865.
34 X. Li, J. Du, W. Xiong and C. Xia, *J. Appl. Phys.*, 2017, **122**, 185702.
35 D. D. Vo, T. V. Vu, A. Kartamyshev, T. H. Ho and N. N. Hieu, *Nanoscale Adv.*, 2024, **6**, 6019–6028.
36 S. Grimme, J. Antony, S. Ehrlich and H. Krieg, *J. Chem. Phys.*, 2010, **132**, 154104.
37 R. Rodrigues Pela, C. Vona, S. Lubeck, B. Alex, I. Gonzalez Oliva and C. Draxl, *npj Comput. Mater.*, 2024, **10**, 77.
38 Y. Xie and P. Kent, *Phys. Rev. B:Condens. Matter Mater. Phys.*, 2013, **87**, 235441.
39 T. Björkman, A. Gulans, A. Krasheninnikov and R. Nieminen, *J. Phys.: Condens. Matter*, 2012, **24**, 424218.
40 T. Björkman, *J. Chem. Phys.*, 2014, **141**, 074708.
41 H. Peng and J. P. Perdew, *Phys. Rev. B*, 2017, **95**, 081105.
42 S. A. Tawfik, T. Gould, C. Stampfl and M. J. Ford, *Phys. Rev. Mater.*, 2018, **2**, 034005.
43 J. Heyd, G. E. Scuseria and M. Ernzerhof, *J. Chem. Phys.*, 2003, **118**, 8207.
44 H. J. Monkhorst and J. D. Pack, *Phys. Rev. B:Condens. Matter Mater. Phys.*, 1976, **13**, 5188.
45 A. Togo, L. Chaput, T. Tadano and I. Tanaka, *J. Phys.: Condens. Matter*, 2023, **35**, 353001.
46 X. Wu, D. Vanderbilt and D. Hamann, *Phys. Rev. B:Condens. Matter Mater. Phys.*, 2005, **72**, 035105.
47 A. M. Ganose, J. Park, A. Faghaninia, R. Woods-Robinson, K. A. Persson and A. Jain, *Nat. Commun.*, 2021, **12**, 2222.
48 L. Cheng and Y. Liu, *J. Am. Chem. Soc.*, 2018, **140**, 17895–17900.
49 S. Demirci, N. Avazlı, E. Durgun and S. Cahangirov, *Phys. Rev. B*, 2017, **95**, 115409.
50 T. V. Vu, N. T. Hiep, V. T. Vi, H. V. Phuc, A. Kartamyshev and N. N. Hieu, *J. Phys. D: Appl. Phys.*, 2025, **58**, 105309.
51 D. Q. Khoa, D. T. Nguyen, C. V. Nguyen, V. T. Vi, H. V. Phuc, L. T. Phuong, B. D. Hoi and N. N. Hieu, *Chem. Phys.*, 2019, **516**, 213–217.
52 D. Zheng, P. Chen, Y. Liu, X. Li, K. Liu, Z. Yin, R. Frisenda, Q. Zhao and T. Wang, *J. Mater. Chem. A*, 2024, **12**, 16952–16986.
53 D. Lu, L. Huang, J. Zhang, Y. Zhang, W. Feng, W. Zeng and Q. Zhou, *ACS Appl. Nano Mater.*, 2023, **6**, 14447–14458.
54 C. Song, S. Huang, C. Wang, J. Luo and H. Yan, *J. Appl. Phys.*, 2020, **128**, 060901.
55 S. Zhou, C.-C. Liu, J. Zhao and Y. Yao, *npj Quantum Mater.*, 2018, **3**, 16.
56 W. Zhang, Y. Ning, H. Li, C. Xu, Y. Wang and Y. Xia, *Nanomaterials*, 2025, **15**, 720.
57 A. J. Garza and G. E. Scuseria, *J. Phys. Chem. Lett.*, 2016, **7**, 4165–4170.
58 Z. A. Moldabekov, M. Lokamani, J. Vorberger, A. Cangi and T. Dornheim, *J. Chem. Phys.*, 2023, **158**, 094105.
59 N. T. Paylaga, C.-T. Chou, C.-C. Lin, T. Taniguchi, K. Watanabe, R. Sankar, Y.-h. Chan, S.-Y. Chen and W.-H. Wang, *npj 2D Mater. Appl.*, 2024, **8**, 12.

60 D. R. Lonsdale and L. Goerigk, *Phys. Chem. Chem. Phys.*, 2020, **22**, 15805–15830.
61 Y.-S. Kim, K. Hummer and G. Kresse, *Phys. Rev. B:Condens. Matter Mater. Phys.*, 2009, **80**, 035203.
62 P. G. Moses, M. Miao, Q. Yan and C. G. Van de Walle, *J. Chem. Phys.*, 2011, **134**, 084703.
63 W. Wan, S. Zhao, Y. Ge and Y. Liu, *J. Phys.: Condens. Matter*, 2019, **31**, 435501.
64 Q. Lu, L. Li, S. Luo, Y. Wang, B. Wang and F.-T. Liu, *RSC Adv.*, 2023, **13**, 18816–18824.
65 S. Grillo, O. Pulci and I. Marri, *Nanomaterials*, 2022, **12**, 2503.
66 H. T. Nguyen, V. T. Vi, T. V. Vu, N. V. Hieu, D. V. Lu, D. Rai and N. T. Binh, *RSC Adv.*, 2020, **10**, 44785–44792.
67 L.-L. Yang, J.-J. Shi, M. Zhang, Z.-M. Wei, Y.-M. Ding, M. Wu, Y. He, Y.-L. Cen, W.-H. Guo, S.-H. Pan, *et al.*, *Chin. Phys. Lett.*, 2019, **36**, 097301.
68 D. K. Sang, H. Wang, M. Qiu, R. Cao, Z. Guo, J. Zhao, Y. Li, Q. Xiao, D. Fan and H. Zhang, *Nanomaterials*, 2019, **9**, 82.
69 X. Qiu, D. Xu, J. Dong, D. Hou, H. Xiong, *et al.*, *Sens. Actuators, A*, 2024, **378**, 115846.
70 X.-Q. Lin, X. Zhang, M.-L. Sun, P.-B. Pan and Y.-G. Yao, *Comput. Theor. Chem.*, 2025, 115281.
71 V. Montes-García and P. Samorì, *Chem. Sci.*, 2022, **13**, 315–328.
72 M. Kaneda, W. Zhang, Z. Liu, Y. Gao, M. Maruyama, Y. Nakanishi, H. Nakajo, S. Aoki, K. Honda, T. Ogawa, *et al.*, *ACS Nano*, 2024, **18**, 2772–2781.
73 X. Tang and L. Kou, *Phys. Status Solidi B*, 2022, **259**, 2100562.
74 L. Zhang, Y. Xia, X. Li, L. Li, X. Fu, J. Cheng and R. Pan, *J. Appl. Phys.*, 2022, **131**, 230902.
75 Y.-P. Chiu, H.-W. Huang and Y.-R. Wu, *Phys. Rev. Appl.*, 2024, **21**, 044046.
76 J. Schmeink, J. Osterfeld, O. Kharsah, S. Sleziona and M. Schleberger, *npj 2D Mater. Appl.*, 2024, **8**, 67.
77 M. A. Mangi, H. Elahi, A. Ali, H. Jabbar, A. B. Aqeel, A. Farrukh, S. Bibi, W. A. Altabey, S. A. Kouritem and M. Noori, *Sens. Actuators Rep.*, 2025, 100302.
78 P. Muralt, R. G. Polcawich and S. Trolier-McKinstry, *MRS Bull.*, 2009, **34**, 658–664.
79 C. Cui, F. Xue, W.-J. Hu and L.-J. Li, *npj 2D Mater. Appl.*, 2018, **2**, 18.
80 F. Mouhat and F.-X. Coudert, *Phys. Rev. B:Condens. Matter Mater. Phys.*, 2014, **90**, 224104.
81 M. Born and K. Huang, *Dynamical Theory of Crystal Lattices*, Oxford university press, 1996.
82 T. Hu and J. Dong, *Phys. Chem. Chem. Phys.*, 2016, **18**, 32514–32520.
83 C. Lee, X. Wei, J. W. Kysar and J. Hone, *Science*, 2008, **321**, 385–388.
84 S. Bertolazzi, J. Brivio and A. Kis, *ACS Nano*, 2011, **5**, 9703–9709.
85 Y. Han, S. Feng, K. Cao, Y. Wang, L. Gao, Z. Xu and Y. Lu, *Cell Rep. Phys. Sci.*, 2020, **1**, 100172.
86 A. Politano and G. Chiarello, *Nano Res.*, 2015, **8**, 1847–1856.
87 S. Thomas, S. Moolayadukkam and K. Priyanka, in *Science and Technology of 2D MoS2*, Springer, 2024, pp. 55–64.
88 B.-F. Qiu, X.-M. Duan, Z. Zhang, X.-Q. Liao, Z.-H. Yang, D.-L. Cai, D.-C. Jia and Y. Zhou, *Rare Met.*, 2020, **39**, 555–561.
89 T.-C. Lim, *SN Appl. Sci.*, 2019, **1**, 176.
90 G. Yang, B. Sun, S. Chen, J. Gu, Y. Shao, H. Wang and K. Yao, *J. Mater. Sci.*, 2017, **52**, 6789–6799.
91 C. Tong and C. Tong, *Advanced Materials for Printed Flexible Electronics*, 2022, pp. 221–255.
92 L. Wang, A. Kutana, X. Zou and B. I. Yakobson, *Nanoscale*, 2015, **7**, 9746–9751.
93 N. T. Hung, A. R. Nugraha and R. Saito, *J. Phys. D: Appl. Phys.*, 2018, **51**, 075306.
94 Q. Cao, X. Geng, H. Wang, P. Wang, A. Liu, Y. Lan and Q. Peng, *Crystals*, 2018, **8**, 357.
95 R. C. Cooper, C. Lee, C. A. Marianetti, X. Wei, J. Hone and J. W. Kysar, *Phys. Rev. B:Condens. Matter Mater. Phys.*, 2013, **87**, 035423.
96 P. Vogl, *J. Phys. C: Solid State Phys.*, 1978, **11**, 251.
97 R. King-Smith and D. Vanderbilt, *Phys. Rev. B:Condens. Matter Mater. Phys.*, 1993, **47**, 1651.
98 R. Resta, *Ferroelectrics*, 1992, **136**, 51–55.
99 K.-A. N. Duerloo, M. T. Ong and E. J. Reed, *J. Phys. Chem. Lett.*, 2012, **3**, 2871–2876.
100 M. N. Blonsky, H. L. Zhuang, A. K. Singh and R. G. Hennig, *ACS Nano*, 2015, **9**, 9885–9891.
101 T. V. Vu, N. T. Hiep, H. V. Phuc, B. D. Hoi, A. Kartamyshev and N. N. Hieu, *Phys. Rev. B*, 2024, **110**, 235403.
102 M. T. Ong, K.-A. N. Duerloo and E. J. Reed, *J. Phys. Chem. C*, 2013, **117**, 3615–3620.
103 M. Noor-A-Alam, H. J. Kim and Y.-H. Shin, *Phys. Chem. Chem. Phys.*, 2014, **16**, 6575–6582.
104 W. Li and J. Li, *Nano Res.*, 2015, **8**, 3796–3802.
105 E. N. Esfahani, T. Li, B. Huang, X. Xu and J. Li, *Nano Energy*, 2018, **52**, 117–122.
106 W. Wu, L. Wang, Y. Li, F. Zhang, L. Lin, S. Niu, D. Chenet, X. Zhang, Y. Hao, T. F. Heinz, *et al.*, *Nature*, 2014, **514**, 470–474.
107 J.-H. Lee, J. Y. Park, E. B. Cho, T. Y. Kim, S. A. Han, T.-H. Kim, Y. Liu, S. K. Kim, C. J. Roh, H.-J. Yoon, *et al.*, *Adv. Mater.*, 2017, **29**, 1606667.
108 F. Wang, J. Jiang, Q. Liu, Y. Zhang, J. Wang, S. Wang, L. Han, H. Liu and Y. Sang, *Nano Energy*, 2020, **70**, 104457.
109 M. Dai, H. Chen, F. Wang, Y. Hu, S. Wei, J. Zhang, Z. Wang, T. Zhai and P. Hu, *ACS Nano*, 2019, **13**, 7291–7299.
110 Y. Zhao, S. Zhang, R. Shi, G. I. Waterhouse, J. Tang and T. Zhang, *Mater. Today*, 2020, **34**, 78–91.
111 H. Wang, X. Zhang and Y. Xie, *Mater. Sci. Eng., R*, 2018, **130**, 1–39.
112 Y. Luo, M. Sun, J. Yu and U. Schwingenschlogl, *Chem. Mater.*, 2021, **33**, 4128–4134.
113 K. Ren, W. Tang, M. Sun, Y. Cai, Y. Cheng and G. Zhang, *Nanoscale*, 2020, **12**, 17281–17289.
114 H. Yao, Q. Wang, J. Li, W. Cai, Y. Wei, B. Wang and J. Wang, *Phys. Chem. Chem. Phys.*, 2020, **22**, 9477–9486.
115 M. Laurien and O. Rubel, *Phys. Rev. B*, 2022, **106**, 045204.

116 V.-A. Ha and F. Giustino, *npj Comput. Mater.*, 2024, **10**, 229.
117 C. Liu, T. Liang, X. Sui, L. Du, Q. Guo, G. Xue, C. Huang, Y. You, G. Yao, M. Zhao, *et al.*, *Nat. Commun.*, 2025, **16**, 544.
118 X. Liu, P. Gao, W. Hu and J. Yang, *J. Phys. Chem. Lett.*, 2020, **11**, 4070–4079.
119 K. Seeger, *Semiconductor Physics*, Springer Science & Business Media, 2013.
120 H. Morkoç and Ü. Özgür, *Zinc Oxide: Fundamentals, Materials and Device Technology*, John Wiley & Sons, 2008.
121 K. L. Kovalenko, S. I. Kozlovskiy and N. N. Sharan, *Phys. Status Solidi B*, 2020, **257**, 1900635.
122 W. Li, S. Poncé and F. Giustino, *Nano Lett.*, 2019, **19**, 1774–1781.
123 L.-B. Shi, S. Cao, M. Yang, Q. You, K.-C. Zhang, Y. Bao, Y.-J. Zhang, Y.-Y. Niu and P. Qian, *J. Phys.: Condens. Matter*, 2019, **32**, 065306.
124 S. Gopalan, G. Gaddemane, M. L. Van de Put and M. V. Fischetti, *Materials*, 2019, **12**, 4210.